Compartmentalized calcium dynamics in a *C. elegans* interneuron encode head movement

Michael Hendricks, **Heonick Ha**, **Nicolas Maffey**, and **Yun Zhang**

Department of Organismic and Evolutionary Biology, Center for Brain Science, Harvard University, Cambridge MA 02138, USA

Abstract

Confining neuronal activity to specific subcellular regions is a mechanism for expanding the computational properties of neurons. While the circuit organization underlying compartmentalized activity has been studied in several systems[1–4], its cellular basis remains elusive. Here, we characterize compartmentalized activity in *Caenorhabditis elegans* RIA interneurons, which display multiple reciprocal connections to head motor neurons and receive input from sensory pathways. We show that RIA spatially encodes head movement on a subcellular scale through axonal compartmentalization. This subcellular axonal activity is dependent on cholinergic input from head motor neurons and is simultaneously present and additive with glutamate-dependent globally synchronized activity evoked by sensory inputs. Postsynaptically, the muscarinic acetylcholine receptor (mAchR) GAR-3 acts in RIA to compartmentalize axonal activity through mobilization of intracellular calcium stores. The compartmentalized activity functions independently from the synchronized activity to modulate locomotory behavior.

The "wiring diagram" of the *C. elegans* nervous system allows dissection of circuit function from single neurons to behavioral outputs[5,6]. RIA interneurons regulate navigation behaviors and occupy a key circuit position, receiving input from multiple sensory networks and displaying reciprocal synaptic connections with head motor neurons (Fig. 1a)[5,7,8]. To characterize the properties of RIA, we expressed the genetically-encoded calcium indicator GCaMP3[9] under the RIA-specific *glr-3* promoter[10] and performed calcium imaging using a microfluidic device in which semi-restrained transgenic animals can bend their heads in the dorsal-ventral plane, allowing simultaneous monitoring of neural activity and head movements[11]. We stimulated the animals with alternating fluid streams of isoamyl alcohol (IAA) and buffer, because IAA is detected by AWC olfactory neurons, one of the sensory neurons upstream of RIA and some of its major synaptic inputs[12]. We did not detect any prominent calcium response in the RIA cell body (Supplementary Fig. 1a). RIA's single axon projects ventrally into the nerve cord, where it forms a hairpin loop, then enters and

extends around the nerve ring, forming a near complete circle (Fig. 1b). *C. elegans* normally lies on its side such that several distinct portions of the RIA axon lie in the same focal plane: the "loop" (the ventrally directed hairpin loop), nrD and nrV (the dorsal and ventral segments of the RIA axon in the nerve ring, respectively) (Fig. 1b). Strikingly, we observed robust calcium dynamics in each of these axonal segments that appeared to be independent, and this axonal calcium activity was correlated with head movement (Fig. 1c, d and Supplementary Movie 1). Calcium transients in nrD were correlated with dorsal head bends while calcium increase in nrV was correlated with ventral head bends. Although another interneuron, AIY, also exhibits calcium signals in its axon, but not soma[12,13], under these conditions the calcium dynamics are synchronized along the entire process (Supplementary Fig. 1b-d).

To quantify the correlation between head movement and RIA calcium dynamics, we defined ventral head deflection as positive and dorsal deflection as negative and performed a cross-correlation analysis between head bending and calcium signals. We found a clear positive correlation between calcium activity in nrV and head movement, whereas calcium dynamics in nrD were negatively correlated with head movement (Fig. 1e). Consistently, calcium responses in nrD and nrV were uncorrelated (Supplementary Fig. 1e). The correlations between nrD and nrV calcium activity and head movement were stimulus-independent, and the correlations were not due to a shared dependence on the stimulus (Supplementary Fig. 1f, g). We also observed distinct calcium transients that occurred synchronously in all three RIA axonal domains (Fig. 1d, filled arrowhead), which will be discussed below. We recorded RIA axonal activity during forward crawling under a cover slip (Supplementary Fig. 2a) and measured GCaMP3 intensity throughout the RIA axon during head bends (Supplementary Fig. 2b). The results consistently showed strong correlations between calcium responses in nrV and nrD with ventral and dorsal head bending, respectively (Supplementary Fig. 2c). Thus, the single RIA axon is partitioned into distinct domains, and calcium dynamics within these domains spatially represent, or encode, head movement.

To investigate how circuit properties regulate RIA compartmentalized activity, we examined the subcellular organization of RIA's synapses within the nerve ring. The majority of these synapses are reciprocal connections with the SMDV and SMDD motor neurons, which innervate ventral and dorsal head muscles, respectively[5]. SMDs also have electrical and chemical synapses with several other head motor neurons that innervate the same muscles and are involved in locomotion[5,7,8]. SMD-RIA synapses are spatially segregated: SMDV synapses onto RIA only in nrV, while SMDD is presynaptic to RIA only in nrD (Fig. 2a). We expressed GCaMP3 in the SMDs using the *glr-1* promoter[14] and recorded calcium activity and head movement. As expected, the calcium responses in SMDV and SMDD were correlated with ventral and dorsal head bending, respectively (Fig. 2b, c and Supplementary Movie 2). Thus, compartmentalized calcium transients in RIA may be driven by SMDs. We also examined calcium responses in animals treated with the nicotinic acetylcholine receptor agonist levamisole. Robust compartmentalized dynamics in RIA and oscillatory dynamics in SMDs persisted in completely paralyzed animals (Fig. 2d, Supplementary Movies 3 and 4). Thus, RIA axonal activity is independent of movement.

Next, we blocked neurotransmission from SMDD and SMDV neurons by expressing tetanus toxin (TeTx) from either the *glr-1* or *lad-2* promoter and examined the effects on RIA activity[15,16]. Both the *glr-1* and *lad-2* promoters drive expression in multiple neurons, but among RIA's presynaptic partners, their expression overlaps only in the SMDs[14,17]. Animals expressing either *glr-1::TeTx* or *lad-2::TeTx* transgene were severely impaired in both nrV and nrD correlations with head movement without losing calcium dynamics, producing synchronized calcium dynamics throughout the RIA neuronal process (Fig. 2e-g). Intracellular cross-correlations between nrV and nrD calcium signals were high in these animals (Fig. 2f, g). TeTx expression in SMDs did not abolish head bending, probably due to functional redundancy with several other motor neurons. Thus, the motor-correlated compartmentalized RIA axonal activity is driven by SMD motor neurons.

Because SMDs are cholinergic, we examined the effect of a hypomorphic mutation, *cha-1(p1152),* in choline acetyltransferase, which is required for biosynthesis of acetylcholine and is expressed in all cholinergic motor neurons[18]. The *cha-1* mutants exhibited active calcium responses in RIA, but were impaired in the correlations between RIA nerve ring calcium dynamics and head bending and defective in compartmentalization of RIA axon (Fig. 3a, b and e). These defects were rescued by a cosmid transgene that contains the *cha-1* genomic locus (Supplementary Fig. 2d). Thus, compartmentalized activity in nrV and nrD and its correlation with head movement require cholinergic neurotransmission.

Most *C. elegans* neurons are predicted to be isopotential[19], making the involvement of postsynaptic ionotropic receptors in generating local calcium changes unlikely. *C. elegans* has a single class of G protein-coupled mAchRs, GAR-1/2/3[20]. When wild type animals were briefly treated with the GAR-3-selective antagonist scopolamine[20], we observed a loss of compartmentalization and head movement correlations and a strong correlation between nrV and nrD dynamics (Fig. 3a, b and e). Scopolamine treatment had no effect on SMD dynamics or their correlation with head movement, demonstrating that the loss of RIA compartmentalization is not due to impaired SMD function (Fig. 3a and Supplementary Fig. 2e). Consistently, the correlation between head movement and RIA axonal activities was abolished in the loss-of-function mutant *gar-3(gk305)*[21] and significantly reduced in *gar-3(vu78)*, which harbors a missense mutation[22]. Both mutants displayed strong correlations between nrV and nrD activity (Fig. 3a, c and e). In contrast, *gar-1(ok755)* mutants did not exhibit defects in RIA calcium responses (Fig. 3c, e). RIA-specific expression of a wild type *gar-3* cDNA in *gar-3(gk305)* mutants significantly rescued these defects (Fig. 3d, f), demonstrating the postsynaptic function of GAR-3 in generating compartmentalization of RIA axonal activity. GAR-3 is similar to the mammalian M1/3/5 mAchRs in both pharmacology and downstream signaling mechanism, which is mediated by $G\alpha_q$ and phospholipase Cβ (PLCβ)[20,23]. There is only one neuronal PLCβ ortholog, EGL-8, in *C. elegans*[24,25]. Consistently, the nonsense mutation in *egl-8(md1971)*[24] exhibited a defect in RIA compartmentalization similar to that in *gar-3(gk305)* mutants (Fig. 3c, e). PLCβ is known to regulate neural activity by activating ER calcium stores. Together, our results are consistent with muscarinic signaling via GAR-3 in RIA mobilizing internal calcium stores via PLCβ to establish compartmentalized axonal activity.

The *gar-3(gk305)* mutant allowed us to selectively test the behavioral consequences of RIA compartmentalized activity, as it does not disrupt synchronous responses or grossly disturb RIA-associated circuitry. We recorded animals during forward locomotion and found that *gar-3(gk305)* mutants generated deeper head bending, leading to a larger amplitude body wave (Fig. 3g). We calculated the mean aspect ratio of an ellipse fit to the animals' posture in each movie frame. The *gar-3(gk305)* mutants exhibited a significantly lower posture aspect ratio than wild type animals, and this defect was fully rescued by expression of a wild type *gar-3* cDNA in RIA (Fig. 3h). Thus, the compartmentalized axonal activity of RIA regulates head movement.

In addition, we observed short, synchronous calcium events across all three RIA axonal compartments (Fig. 1d). We examined the temporal distribution of these events by defining synchronous calcium influx and efflux events as time points at which the rate of change in GCaMP3 intensity in all three compartments was positive and negative, respectively. We subjected animals to alternating streams of buffer and IAA and scored synchronous events in the raster plot shown in Fig. 4a. We calculated the mean rate of calcium flux across all three axonal domains (time histogram in Fig. 4a). Two trials per animal were averaged to generate the time histograms shown in Fig. 4b. Removal of IAA (IAA-off) evoked synchronous calcium influx followed by synchronous efflux (filled arrowhead and open arrow, respectively in Fig. 4a). In contrast, switching from buffer to IAA (IAA-on) elicited a high frequency of synchronous calcium efflux events followed by influx (open arrowhead and filled arrow in Fig. 4a). Thus, global RIA axonal activity is transiently suppressed by IAA presentation and activated by its removal.

IAA is sensed by the AWC olfactory sensory neurons and sensorimotor responses to IAA require glutamatergic neurotransmission[12]. Mutants defective in the vesicular glutamate transporter EAT-4 displayed a complete loss of IAA-evoked activity in RIA (Fig. 4b, c), which was rescued by an *eat-4* transgene (Supplementary Fig. 3a). Motor-correlated compartmentalized RIA axonal dynamics were maintained in the *eat-4* mutants (Supplementary Fig. 3b). Blocking synaptic release from SMDs did not disrupt synchronous responses (Supplementary Fig. 4). Thus, sensory-evoked synchronous activity in RIA is regulated independently from the motor neuron inputs into nrV and nrD compartments. The synchronous and compartmentalized calcium dynamics in RIA may be either simultaneous and additive or mutually exclusive. To distinguish between these possibilities, we challenged RIA with high-frequency alternating stimuli (0.25 Hz) to see if head movement correlations were maintained against rapid synchronous activity. Fast switching caused synchronous calcium dynamics in phase with the stimuli, the spectral profiles of nrV and nrD calcium signals showed 0.25 Hz peaks corresponding to the stimulus, and correlations between nrV and nrD and head movement appeared reduced (Fig. 4d, e). After subtraction of the synchronous component from each compartment, the correlations between head movement and nrV and nrD activity were restored (Fig. 4e), demonstrating that the calcium signals measured in each RIA axonal compartment represent the combined signals of sensory-evoked and motor inputs.

There are two primary means for the nervous system to monitor its own output: proprioceptive feedback, which responds to the mechanical stimuli produced by self-motion,

and corollary discharge (CD), in which a copy of the motor command is transmitted to sensory processing networks[26]. RIA compartmentalized dynamics exhibit key features of CD: they originate from the motor system, represent spatial attributes of the behavior, and modulate the encoded behavior. Several *C. elegans* behaviors require detection of spatial changes in stimuli relative to head movement. Network models for these behaviors have been proposed, however, the potential underlying circuit mechanisms have not been observed *in vivo*[27]. Our identification of CD from head motor neurons to interneurons adds an important property to the navigation network, whereby a sensorimotor circuit can monitor self-motion via CD and integrate motor dynamics with sensory stimuli to regulate locomotion (Supplementary Fig. 5).

Compartmentalization is a feature of morphologically complex cells, such as vertebrate starburst amacrine cells[1] and fly tangential cells[28]. The existence of compartmentalization within the unbranched axon of a unipolar neuron in *C. elegans* suggests a deeply conserved mechanism for signal processing. Interestingly, our identification of a cholinergic pathway establishing RIA compartmental activity agrees with observations in inhibitory thalamic interneurons, where cholinergic input regulates the dynamic coupling between distal dendrites and the rest of the neuron[4]. These comparisons suggest commonalities in the signaling and circuit properties underlying compartmentalization. Our findings provide a framework for sensorimotor processing and integration at the subcellular level and a mechanism underlying functional specificity of circuit connections among *C. elegans* neurons, many of which are isopotential, thus revealing a new perspective on the network topology of the nematode nervous system.

METHODS SUMMARY

Strains were maintained under standard conditions[29]. Transgenesis[30] and calcium imaging[7,11,12] were performed as described. Cross-correlations and statistical analyses were performed using JMP8 (SAS). Time series data were filtered by exponential smoothing, an instantaneous time derivative calculated for each frame, and these data were used for cross-correlation with +/− 50 time lags (+/− 10 sec). To detect synchronous calcium peaks, we scored synchronous events and calculated the mean rate of calcium flux as described in the text. Locomotion analysis was done on NGM agar without food using a 5 megapixel camera at 2 frames per second.

Methods

Strains

C. elegans strains were maintained under standard conditions[29]. The following strains were used in this study: N2 (Bristol), ZC1507 *yxIs18 [Pglr-3a::GCaMP3.3, Punc-122::dsred]*, ZC1508 *yxIs19 [Pglr-3a::GCaMP3.3, Punc-122::dsred]*, ZC1148 *yxIs1[Pglr-1::GCaMP3.3, Punc-122::gfp]*, ZC1591 *yxIs19; yxEx778 [Plad-2::TeTx:mCherry, Punc-122::gfp]*, MT6308 *eat-4(ky5)*III, PR1152 *cha-1(p1152)*IV, ZC1576 *cha-1(p1152)*IV; *yxIs19*, ZC1598 *eat-4(ky5)*III; *yxIs19*, ZC1563 *yxIs19; yxEx749 [Pglr-1::TeTx:mCherry, Punc-122::gfp]*, ZC1626 *eat-4(ky5)*III; *yxIs19; yxEx802 [Peat-4::eat-4, Punc-122::gfp]*, ZC1633 *cha-1(p1152)*IV; *yxIs19; yxEx809 [cosmid ZC416,*

Punc-122:gfp], RM2221 *egl-8(md1971)*V, ZC1922 *egl-8(md1971)*V*; yxIs19*, VC657 *gar-3(gk305)*V, JD217 *gar-3(vu78)*V, ZC1790 *gar-1(ok755)*X*; yxIs19*, ZC1792 *gar-3(gk305)*V*; yxIs19*, ZC1834 *gar-3(vu78)*V*; yxIs19*, ZC1923 *gar-3(gk305)*V*; yxIs19; yxEx968 [Pglr-3::gar-3]*.

Molecular biology

The genetically encoded calcium indicator *GCaMP3.3*[9] (gift of L. Looger and L. Tian) was cloned upstream of the 3' untranslated region of the *unc-54* gene in pSM_Not (gift of C. Bargmann) and a Gateway recombination cassette (rfB) (Invitrogen) was ligated upstream of *GCaMP3.3* to produce *pSM-rfB-GCaMP3.3*. The *GCaMP3.3* sequence was replaced with a tetanus toxin-mCherry fusion (gift of C. Bargmann) to produce *pSM-rfB-TeTx:mCherry*, or with a full-length *gar-3* cDNA (gift of Y. Kohara) to produce *pSM-rfB-gar-3*. The rfB cassette was also cloned upstream of *eat-4* cDNA (gift of C. Bargmann) to produce *pSM-rfB-eat-4*. A 5.3 kb genomic fragment upstream of the *glr-1* gene (forward primer ACTGACCACTGCAGCATTTT, reverse TGTGAATGTGTCAGATTGGG), 2.8 kb upstream of *glr-3* (forward TCGGAAATGCGGAAGTTCTT, reverse ATGTTAATAGCAAATATTGAAG) and 5.5 kb upstream of *eat-4* (forward TTGTCCACATTCTAGTAG, reverse GGTTTCTGAAAATGATGATG) were amplified by PCR and cloned into the pCR8 Gateway entry vector (Invitrogen). Recombination reactions were performed according to the manufacturer's instructions, producing *Pglr-3::GCaMP3.3, Pglr-1::GCaMP3.3, Pglr-1::TeTx:mCherry, Plad-2::TeTx:mCherry* and *Peat-4::eat-4*. A PCR product comprising 1.2kb of the *glr-3* upstream sequence (*Pglr-3a*), *GCaMP3.3*, and the *unc-54* 3'UTR (forward GCCAGAGATGAGCATGATTC, reverse CGGCCGACTAGTAGGAAACA) was used at 50 ng/μL for germline transformation. For *cha-1* genomic rescue, cosmid ZC416 (Wellcome Trust Sanger Institute, UK) was injected at 10 ng/μL. Other plasmids were injected at 25 ng/μL. Either *Punc-122::gfp* or *Punc-122::dsred* was used as a coinjection marker for all lines. Microinjection was performed as described[30]. Integration of extrachromosomal arrays was performed by gamma irradiation as described by the Hobert Lab. Mutant lines were provided by the *Caenorhabditis* Genetics Center. For RIA imaging in mutant backgrounds, mutants were crossed to strain ZC1508 and F2 progeny were selected for homozygosity for both the integrated transgene and mutation of interest.

Calcium imaging

Calcium imaging was performed in a microfluidic device essentially as described[11,12]. Fluorescence time lapse imaging (100 msec exposures, 5 Hz) was performed on a Nikon Eclipse Ti-U inverted microscope with a 40x oil immersion objective and a Photometrics CoolSnap EZ camera. Animals were presented with alternating streams of NGM buffer (1 mM $CaCl_2$, 1 mM $MgSO_4$, 25 mM KPO_4) and 10^{-4} isoamyl alcohol in NGM buffer, a concentration shown to be optimal for activating AWC[12]. All image analysis was performed using NIH ImageJ and frames were aligned using the StackReg plugin. After background subtraction, total fluorescence intensity was measured from individual ROIs corresponding to subcellular domains in the case of RIA or the entire cell body for other neurons. For RIA, intensity values for each ROI were linearly scaled from 0 to 1 using the formula ($F - F_{min})/(F_{max} - F_{min}$). Freely moving animals on *E. coli* OP50 lawns were lightly compressed

with a cover slip and imaged under a 10x objective with 10 msec exposures at 5 Hz. Frames were chosen in which the animal's head was deflected dorsally or ventrally. A linear ROI tracing the RIA process was used to generate an intensity profile. Where noted, animals were treated with 2 mM levamisole (Tetramisole HCl, Sigma L9756) or 100 μM scopolamine (Sigma S1875) immediately prior to and during imaging.

Head movement quantitation

An ROI comprising the mobile portion of the animal's head and centered on its midline was selected and binarized. A macro in ImageJ was used to calculate head displacement from the ROI centre in the dorsal-ventral plane normalized relative to the maximum deflection (in either direction). Briefly, a centre of mass was defined as the mean pixel position along the DV axis. The difference between the centre of mass and the position of the midline was calculated for each frame. This gave an index between -1 and 1; ventral was defined as positive.

Correlation analysis

Cross-correlations and all statistical analyses were performed using JMP8 software (SAS). Fluorescence intensity and head position time series data were filtered by exponential smoothing ($\alpha = 0.3$), an instantaneous time derivative calculated for each frame, and these data were used for cross-correlation with $+/-$ 50 time lags ($+/-$ 10 sec). For comparison of peak correlations, the maximum correlation (positive or negative) in a 1 second time window centered on the peak of the control mean correlation was used. Mutants and transgenic animals were compared by analysis of variance (ANOVA) with wild type or non-transgenic siblings.

Analysis of synchronous calcium events

To detect short-term synchronous calcium peaks, we scored each time point in which the nrV, nrD and loop regions all had time derivatives greater than 0 (influx) or less than 0 (efflux) as a synchronous event (raster plot in Fig. 4a). At each of these time points, the mean rate of calcium flux (positive or negative) was calculated; time points without synchronous activity were scored 0. The mean rate of change across all animals was calculated at each time point. For each animal, a set of two IAA-on events and two IAA-off events were scored by comparing a 1-second time window just prior to the stimulus switch to a 1-second time window centered on the time point exhibiting peak response in wild type animals. ANOVA with repeated measures was used to compare within-group responses to stimulus presentation and removal, and between-group differences were evaluated by testing for significant interactions between stimulus response and genotype.

Behavior

All analysis was done in ImageJ. Well-fed adult animals were washed twice briefly in NGM buffer and transferred to a 90 mm NGM agar petri plate with no food. The entire plate was imaged with a 5 megapixel camera (JAI) with a 60 mm lens (AF Micro-Nikkor, Nikon) using LabVIEW (National Instruments) at 2 frames/s for several minutes. For each animal, 100 frames of video (50 s) were analyzed. An ellipse was fit to a spline corresponding to the

animal's midline, and the aspect ratio of this ellipse was used as a size-independent index of the animal's posture, in which lower values indicate higher amplitude and lower wave length gait. Frames in which animals were not performing forward locomotion ($< 2\%$) were excluded.

Connectomics

Network graphs were drawn using Cytoscape based on serial electron microscopy[5,6].

Supplementary Material

Refer to Web version on PubMed Central for supplementary material.

Acknowledgments

References

1. Euler T, Detwiler PB, Denk W. Directionally selective calcium signals in dendrites of starburst amacrine cells. Nature. 2002; 418:845–852. [PubMed: 12192402]

2. Borst A, Euler T. Seeing things in motion: Models, circuits, and mechanisms. Neuron. 2011; 71 : 974–994. [PubMed: 21943597]

3. Rall W, Shepherd GM, Reese TS, Brightman MW. Dendrodendritic synaptic pathway for inhibition in the olfactory bulb. Exp Neurol. 1966; 14:44–56. [PubMed: 5900523]

4. Zhu J, Heggelund P. Muscarinic regulation of dendritic and axonal outputs of rat thalamic interneurons: a new cellular mechanism for uncoupling distal dendrites. J Neurosci. 2001; 21:1148–59. [PubMed: 11160385]

5. White JG, Southgate E, Thomson JN, Brenner S. The structure of the nervous system of the nematode *Caenorhabditis elegans*. Phil Trans R Soc Lond B. 1986; 314:1–340. [PubMed: 22462104]

6. Varshney LR, Chen BL, Paniagua E, Hall DH, Chklovskii DB. Structural properties of the *Caenorhabditis elegans* neuronal network. PLoS Comput Biol. 2011; 7:e1001066. [PubMed: 21304930]

7. Ha HI, et al. Functional organization of a neural network for aversive olfactory learning in *Caenorhabditis elegans*. Neuron. 2010; 68:1173–1186. [PubMed: 21172617]

8. Gray JM, Hill JJ, Bargmann CI. A circuit for navigation in *Caenorhabditis elegans*. Proc Natl Acad Sci USA. 2005; 102:3184–3191. [PubMed: 15689400]

9. Tian L, et al. Imaging neural activity in worms, flies and mice with improved GCaMP calcium indicators. Nat Methods. 2009; 6:875–881. [PubMed: 19898485]

10. Brockie PJ, Madsen DM, Zheng Y, Mellem J, Maricq AV. Differential expression of glutamate receptor subunits in the nervous system of *Caenorhabditis elegans* and their regulation by the homeodomain protein UNC-42. J Neurosci. 2001; 21:1510–1522. [PubMed: 11222641]
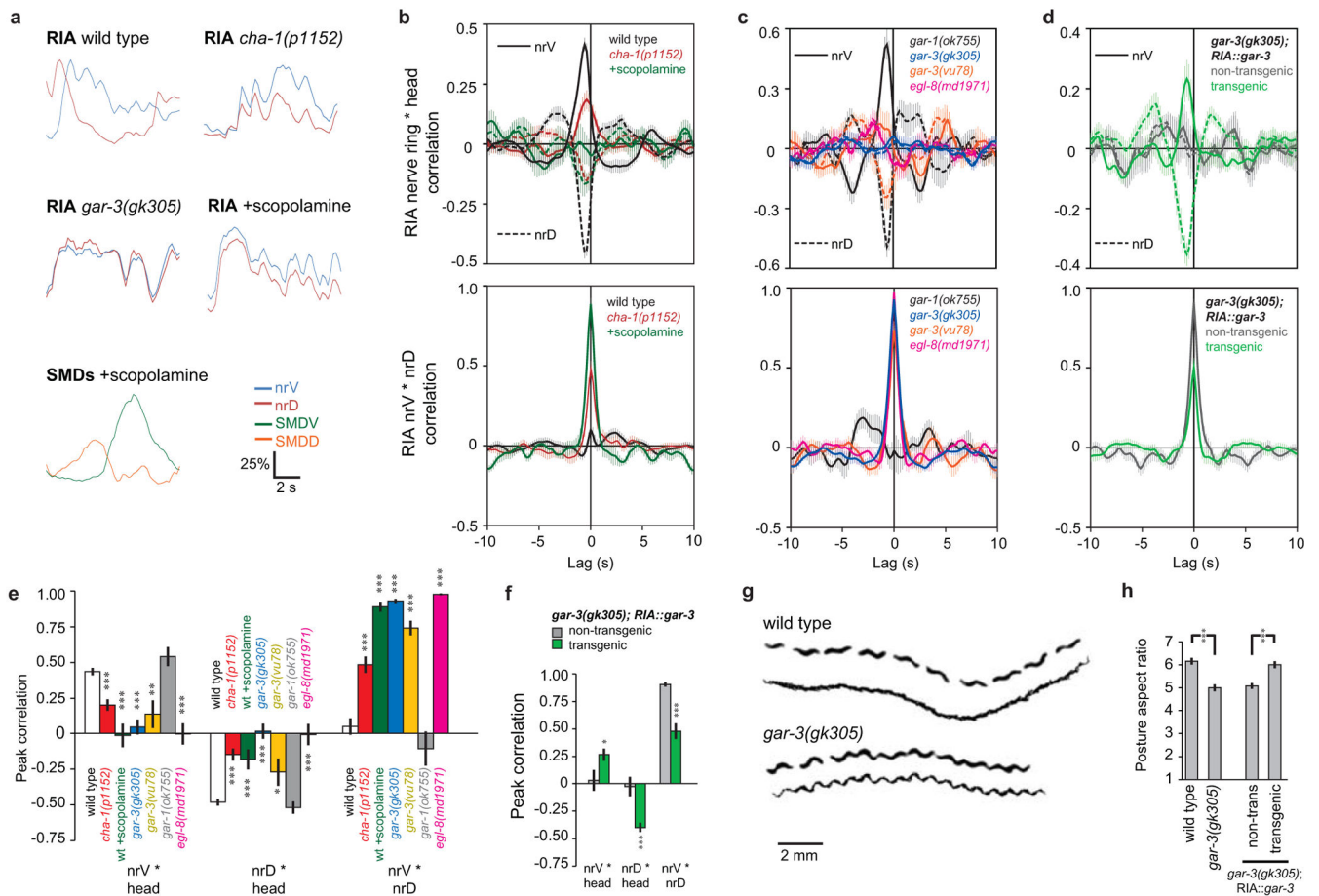
11. Chronis N, Zimmer M, Bargmann CI. Microfluidics for in vivo imaging of neuronal and behavioral activity in *Caenorhabditis elegans*. Nat Methods. 2007; 4:727–731. [PubMed: 17704783]

12. Chalasani SH, et al. Dissecting a circuit for olfactory behaviour in *Caenorhabditis elegans*. Nature. 2007; 450:63–70. [PubMed: 17972877]

13. Clark DA, Biron D, Sengupta P, Samuel ADT. The AFD sensory neurons encode multiple functions underlying thermotactic behavior in *Caenorhabditis elegans*. J Neurosci. 2006; 26:7444–7451. [PubMed: 16837592]

14. Hart AC, Sims S, Kaplan JM. Synaptic code for sensory modalities revealed by *C. elegans* GLR-1 glutamate receptor. Nature. 1995; 378:82–85. [PubMed: 7477294]

15. Macosko EZ, et al. A hub-and-spoke circuit drives pheromone attraction and social behaviour in *C. elegans*. Nature. 2009; 458:1171–1175. [PubMed: 19349961]

16. Schiavo G, et al. Tetanus and botulinum-B neurotoxins block neurotransmitter release by proteolytic cleavage of synaptobrevin. Nature. 1992; 359:832–835. [PubMed: 1331807]

17. Wang X, et al. The *C. elegans* L1CAM homologue LAD-2 functions as a coreceptor in MAB-20/Sema2 mediated axon guidance. J Cell Biol. 2008; 180:233–246. [PubMed: 18195110]

18. Rand, JB.; Nonet, ML. Synaptic transmission*C. elegans II*. Riddle, DL.; Blumenthal, T.; Meyer, BJ.; Priess, JR., editors. Vol. 22. Cold Spring Harbor Laboratory Press; 1997. p. 1049-1052.

19. Goodman MB, Hall DH, Avery L, Lockery SR. Active currents regulate sensitivity and dynamic range in *C. elegans* neurons. Neuron. 1998; 20:763–772. [PubMed: 9581767]

20. Park YS, Kim S, Shin Y, Choi B, Cho NJ. Alternative splicing of the muscarinic acetylcholine receptor GAR-3 in *Caenorhabditis elegans*. Biochem Biophys Res Commun. 2003; 308:961–965. [PubMed: 12927813]

21. Liu Y, LeBoeuf B, Garcia LR. G alpha(q)-coupled muscarinic acetylcholine receptors enhance nicotinic acetylcholine receptor signaling in *Caenorhabditis elegans* mating behavior. J Neurosci. 2007; 27:1411–1121. [PubMed: 17287516]

22. Steger KA, Avery L. The GAR-3 muscarinic receptor cooperates with calcium signals to regulate muscle contraction in the *Caenorhabditis elegans* pharynx. Genetics. 2004; 167:633–643. [PubMed: 15238517]

23. Hulme EC, Birdsall NJ, Buckley NJ. Muscarinic receptor subtypes. Annu Rev Pharmacol Toxicol. 1990; 30:633–673. [PubMed: 2188581]

24. Miller KG, Emerson MD, Rand JB. Goalpha and diacylglycerol kinase negatively regulate the Gqalpha pathway in *C. elegans*. Neuron. 1999; 24:323–333. [PubMed: 10571227]

25. Lackner MR, Nurrish SJ, Kaplan JM. Facilitation of synaptic transmission by EGL-30 Gqalpha and EGL-8 PLCbeta: DAG binding to UNC-13 is required to stimulate acetylcholine release. Neuron. 1999; 24:335–346. [PubMed: 10571228]

26. Crapse TB, Sommer MA. Corollary discharge across the animal kingdom. Nat Rev Neurosci. 2008; 9:587–600. [PubMed: 18641666]

27. Lockery SR. The computational worm: spatial orientation and its neuronal basis in *C. elegans*. Curr Opin Neurobiol. 2011; 21:782–790. [PubMed: 21764577]

28. Joesch M, Schnell B, Raghu SV, Reiff DF, Borst A. ON and OFF pathways in *Drosophila* motion vision. Nature. 2010; 468:300–304. [PubMed: 21068841]

29. Brenner S. The genetics of *Caenorhabditis elegans*. Genetics. 1974; 77:71–94. [PubMed: 4366476]

30. Mello CC, Kramer JM, Stinchcomb D, Ambros V. Efficient gene transfer in *C. elegans*: extrachromosomal maintenance and integration of transforming sequences. EMBO J. 1991; 10:3959–3970. [PubMed: 1935914]
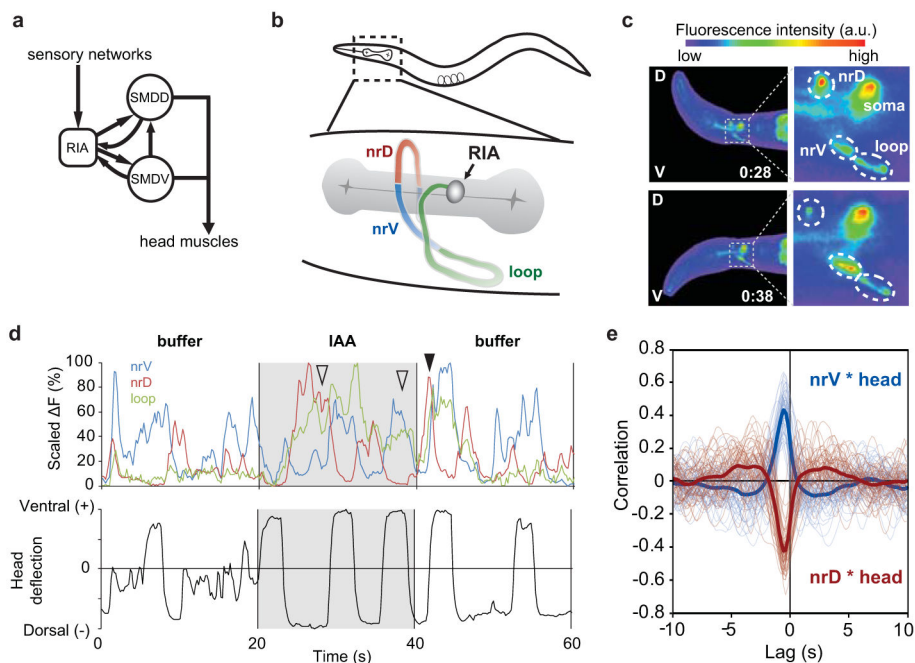
Figure 1. Compartmentalized calcium signals in RIA encode head movement
a, Highly simplified RIA and SMD synaptic connections. **b,** RIA anatomy showing nrD, nrV and loop subdomains. **c,** Single frames of GCaMP3 fluorescence recording in RIA. Dashed ovals denote subdomains in **b.** Anterior, left; D, dorsal; V, ventral. **d,** Calcium dynamics in RIA axonal domains and corresponding head bending. Open arrowheads, time points in **c**; filled arrowhead, a synchronous calcium event. **e,** Cross-correlations between nrV or nrD Ca^{2+} responses and head movement. Gray lines, individual animals (n = 53); solid lines, mean values.

Figure 2. RIA compartmentalized activity requires transmission from SMD motor neurons
a, Topography of SMD synapses onto RIA and muscles. **b,** Overlay of representative SMD calcium recording and movement. The SMDD trace is inverted to show correlation with dorsal head bending. **c,** Cross-correlations of SMDV/D with head movement (n = 8). **d,** Representative calcium recordings of RIA subdomains or SMDs in levamisole-treated animals. **e,** RIA correlations with head movement in *glr-1::TeTx* or *lad-2::TeTx* transgenic strains (*glr-1* n = 18, *lad-2* n = 17, control n = 28). **f,** Internal cross-correlations in SMD::TeTx strains. **g,** Comparison of peak correlations between strains. Cross-correlation plots and bar charts are mean +/− s.e.m.. ***p < 0.001, **p < 0.01, ANOVA corrected for multiple comparisons.

Figure 3. A muscarinic acetylcholine pathway establishes motor-correlated RIA dynamics
a, Sample calcium dynamics of nrV, nrD, and SMDs. **b,** Cross-correlations between RIA dynamics and head movement and internal cross-correlations in *cha-1(p1152)* (n = 18, control n = 25) and scopolamine-treated wild type animals (100 μM, n = 10). **c,** Cross-correlation plots as in **b** for mutants: *gar-1(ok755)* (n = 5), *gar-3(gk305)* (n = 16), *gar-3(vu78)* (n = 6), *egl-8(md1971)* (n = 7). **d,** Cross-correlations of transgenic (n = 13) and nontransgenic (n = 9) siblings in a strain expressing a *gar-3* cDNA in RIA in *gar-3(gk305)* mutants. **e, f,** Peak correlation comparisons for data in **b-d. g,** Images of wild type and *gar-3(gk305)* animals every 5 seconds over 50 seconds, beneath each image series is the projection of each animal's midline every 0.5 seconds over the same time period. **h,** Comparison of mean postural aspect ratios during forward locomotion for wild type (n = 17), *gar-3(gk305)* (n = 10) and transgenic (n = 10) and non-transgenic (n = 15) siblings in the RIA::*gar-3* rescue line. Cross-correlation plots and bar charts are mean +/− s.e.m. ***p < 0.001, **p < 0.01, *p < 0.05, ANOVA corrected for multiple comparisons.
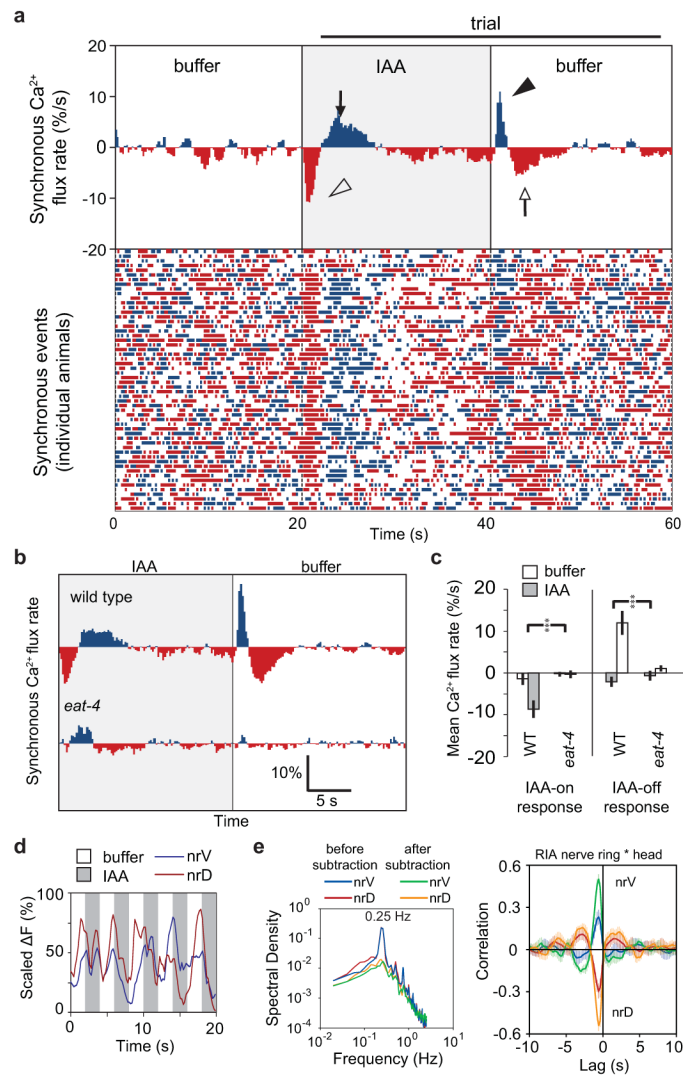
Figure 4. Sensory-evoked synchronized RIA activity is dependent on glutamatergic transmission and is additive with compartmentalized dynamics

a, , Raster plot and histogram of synchronous calcium influx (blue) or efflux (red). Dots, synchronous events; histogram, mean rate of Ca^{2+} flux (n = 53). **b, c**, Mean responses across two trials in wild type (n = 19) and *eat-4(ky5)* mutants (n = 18). ***p < 0.001, significant interaction between stimulus response and genotype, MANOVA with repeated measures. Error bars, s.e.m. **d**. Example of nrV and nrD responses to switching between IAA and buffer every 2 seconds. **e**, Spectral density of nrV and nrD activity and cross-correlations (mean +/− s.e.m.) between nrV or nrD and head movement before and after synchronous signal subtraction (see text).